RSC Advances

ROYAL SOCIETY OF CHEMISTRY

www.rsc.org/advances

Electro-catalytic degradation pathway and mechanism of acetamiprid using Er doped Ti/SnO_2–Sb electrode

Shanping Li[a, b,*], Yahui Li[a], Xueyuan Zeng[a], Wenran Wang[a], Ruoxin Shi[a], Lina Ma[a]

a. School of Environmental Science and Engineering, Shandong University, 27 Shandananlu, Jinan, 250100, China.

b. Shandong Key Laboratory of Water Pollution Control and Resource Reuse, Jinan, 250100, China

E-mail: lishanping@sdu.edu.cn

Corresponding author. Professor Shanping Li Tel.:+86 0531-88362872; fax: +86 0531-88362872

Abstract

The acetamiprid, one kind of new neonicotinoid pesticides, shows a high threat to water system. Electro-catalytic degradation of acetamiprid was evaluated at Er doped Ti/SnO_2–Sb electrode prepared by Pechini's method. The acetamiprid degradation obeyed the first order reaction kinetics and was controlled by mass transport and oxygen evolution. TOC removal efficiency and UV scan curves revealed that some intermediate products were produced by the Er doped Ti/SnO_2–Sb electrode. Through electrospray ionization quadrupole time-of-flight tandem mass spectrometry, we got ion mass-to-charge ratio of intermediate products. Combining the experimental results, one degradation pathway was proposed for electro-catalytic degradation of acetamiprid. Electrodes were mainly characterized by linear sweep voltammetry and cyclic voltammetry. The acetamiprid and TOC concentrations were reduced in 87.45 % and 69.31 %, respectively, after 180 min of electrolysis at 10 mA cm^{-2}.

Keywords: Acetamiprid; 6-Chloronicotinic acid; Er; Electro-catalytic degradation.

1. Introduction

Electro-catalytic (EC) processes have attracted more sizeable interests in recent years, because they were promising, highly efficient methods for degrading pollutants and could be operated essentially under largely similar conditions for a wide variety of wastewater [1-6].The key factor of EC wastewater treatment is the nature of the electrode used in the process. Dimensionally stable anodes (DSAs) have been used for some years, and substrate of the electrode is generally titanium depositing of a thin layer of metal oxides, e.g., RuO_2 [7], IrO_2 [8], PbO_2 and SnO_2 [5,9-11]. Although

RuO_2 and IrO_2 electrodes have been widely applied in chlorine-alkali industry, but the prices of metal oxides were higher and the electrodes didn't show a high efficiency for organic oxidation. PbO_2 electrodes studied by some researchers [5, 12, 13] showed a highly effective EC capacity for organic oxidation, however the working electrode might dissolve Pb^{2+} causing the secondary pollution of water. Electrodes based on the SnO_2 also reflected a similar capacity for organic oxidation as PbO_2 electrode and had a high oxygen evolution over-potential [14, 15]. Because of its high electrical resistance, SnO_2 electrode was often doped with Sb to improve its electrical conductivity, and SnO_2-Sb electrodes presented well EC activities and organic oxidation rates [16]. Recent years, there were attempts to dope the SnO_2-Sb electrodes with rare earth elements, such as Nd, Gd, Eu and so on, in order to furtherly improve the performance of SnO_2-Sb electrode in an EC process [3,17,18]. Phenol degradation rate was increased up to 41 % as a result of moderate Gd adding into the Ti/SnO_2-Sb electrode [3]. Moderate Eu doped Ti/SnO_2-Sb electrode could produce smaller grain sizes of SnO_2 resulting in larger surface areas and active sites on the electrode surface improving EC oxidation [18].

New neonicotinoid pesticides are a new class of chemical pesticides and also the fourth class of pesticides after organophosphorus pesticides, pyrethroid pesticides and carbamate pesticides. At present, they have been registered in more than 120 countries maintaining a rapidly increasing application.

Acetamiprid (ACT) was exploited in 1996 by NIPPON SODA CO., LTD. ACT was widely used in agriculture and horticulture to control sucking insects, and there were about 400 companies registering and producing ACT in China. The ACT has a high water soluble (The solubility is 4200 mg L-1 in water at a temperature 293 K and pH=7), and is of great stability in the sun and weak acidic medium. After accumulation in pure water, it is difficult to be degraded through hydrolysis or photolysis, which would cause environmental pollution and bring on health risk for human. According to the article [19], 6-Chloronicotinic acid (6-CNA) was regarded as the degradation product for ACT by photocatalytic oxidation. 6-CNA is mainly used as pharmaceutical intermediate. After absorbed by mankind, it could combine with serum albumin causing a serious threat to human health [20]. The chemical structures of the ACT and 6-CNA are presented in Fig. 1.

Recent studies have mainly reported the removal of neonicotinoid pollutants by photolytic/photocatalytic oxidation [21- 23]. So studying the EC degradation of ACT

would provide a treatment or pre-treatment method, and enrich research on the new neonicotinoid pesticides.

In the paper, the objective of this study was analyzing intermediates and products for EC degradation ACT by means of electrospray ionization quadrupole time-of-flight tandem mass spectrometry (ESI-Q-TOF-MS), proposing the EC degradation pathway of ACT in aqueous solution. The degradation kinetics of ACT removal at different initial concentrations was further investigated. Several calcination temperatures were used to prepare electrodes by Pechini's method and electrochemical prosperities of working electrode prepared by ourselves were evaluated by LSV and CV.

2. Experimental

2.1 Electrode preparation

Ti meshes, which were chosen as the substrate for oxide-coated electrodes, were rectangular in shape. The size of diamond meshes was 3 mm × 8 mm. They were polished thoroughly with mechanical polishing, degreased in boiling 5 % Na_2CO_3 for 1 h, and then etched in boiling 10 % oxalic acid for 2 h followed by thorough washing with distilled water. The treated Ti meshes became grey, lost their metallic sheen and preserved in 95 % ethanol.

The electrodes were covered with rare earth Er doped SnO_2-Sb film prepared by Pechini's method. The preparation procedure is similar as described in our previous report and elsewhere [24, 25]. The metal: citric acid (CA) : ethylene glycol (EG) mole ratio were 1: 3: 10. Briefly, CA was dissolved into EG under 65 ℃ with stirring named as solution A. $SnCl_4$•$5H_2O$, $SbCl_3$ and Er were added into the solution A. Heat the mixed solution up to 90 ℃ with stirring for 30min to get precursor solutions. The Sn/ Sb/ Er molar ratios was 100: 6: 0.5. The pre-treatment of Ti meshes were dipped into precursor solution, then dried in an electric oven at 130 ℃ for 30 min. After four cycles of both dipping and drying, the electrode covered by the metals film was heated in a muffle oven with a heating rate of 10 ℃ min^{-1} to 550 ℃ and kept at 550 ℃ for 30 min for coating pyrolysis. This whole process (dipping, drying and pyrolysis) was repeated 3 times and finally, the electrodes were calcinated at a variable temperature of 550 ℃, 600 ℃, 650 ℃, 700 ℃ or 750 ℃ for 2 h with a heating rate of 5 ℃ min^{-1} respectively. In this work, all chemicals were of reagent grade. The scheme of citric acid chelate precursor method for electrode preparation is

shown in Fig. S10.

2.2 Analytical methods

Thermal analyzer (SDT Q600, TA, America) was employed to monitor the changes of the containing Er precursor's temperature and weight to reflect the change of material and the formation of phase in the process of electrode calcination stage. There were some analysis conditions, namely, the temperature ranged from 25 ℃ to 800 ℃, the heating rate was 10 ℃ min^{-1}, and the testing atmosphere was air. Before testing, the containing Er precursor was dried at 130 ℃ for 30 min to get a xerogel.

The precursor solution was dried, heat treatment, and calcinated at 650 ℃ to obtain precursor powder. The diffuse reflection spectrum of precursor powder was recorded by UV/Vis/NIR diffuse reflectance spectroscopy (UV-3600, Shimadu). Diffuse scanning ranged from 230 nm to 800 nm, and the control and analysis software is UV Probe 2.10.

The concentration of ACT during the EC degradation process was established by an UV-spectrometer (TU-1810PC, Beijing Purkinje General Instrument Co. Ltd, China). The 245 nm peak was used in preference.

The organic concentration in the solution, was measured by a total organic carbon (TOC) analyzer (TOC-5000A, Shimadu) based on the combustion-infrared method.

Electrospray ionization quadrupole time-of-flight tandem mass spectrometry (ESI-Q-TOF-MS, Agilent, America) was used for the measurement intermediate. Before injecting the sample into the ESI-Q-TOF-MS, the sample was extracted with ethanol. Obtain the ion peak of $[M+H]^+$ or $[M-H]^-$ to analyze the degradation products in the ESI ionization source mode.

2.3 Electrochemical characterization of electrode

Electrochemical measurements were carried out using an electrochemical workstation (CHI700B, Shanghai Chenhua, China) in a three-compartment cell. The self-made electrode (10 mm × 10 mm) was used as the working electrode, a Ti plate electrode (20 mm × 30 mm) was employed as the counter electrode, and a saturated calomel electrode (SCE) was used as the reference electrode (all the electrode potentials in this paper are in reference to this electrode).

The linear sweep voltammetry (LSV) tests were employed to analyze oxygen evolution potential of the self-made electrodes. The solution contained 0.5 M Na_2SO_4.

Scanning voltage ranged from -2 V to 3 V with a scan rate of 20 mV s^{-1}.

The kinetic of the oxygen evolution reaction (OER) was studied in terms of Tafel plot, which has sometimes been referred to as "the first law of electrode kinetics" [26], namely

$$\eta = a + b\,logi \quad (1)$$

Where a (V) is the overpotential value under unit of the current density, b (V) is the Tafel slope, and i (mA cm^{-2}) is the current density.

The cyclic voltammetry (CV) experiments were conducted to inspect the reaction characteristics and mechanisms of anode preliminary [27]. The solution contained either 0.5 M Na_2SO_4 or 0.5 M Na_2SO_4 containing 25mg L^{-1} ACT (Na_2SO_4 is as electrolyte). Cycling between 0.5 V and 2.5 V with a scan rate of 50 mV s^{-1} obtained the CV diagram.

2.4 Electrochemical experiment for ACT and 6-CNA

Taking ACT and 6-CNA as model organic compounds, EC experiments were conducted in a batch of electrolysis cells that were 150 ml beakers made of glass. For each cell, a prepared anode (30 mm × 40 mm) and a Ti plate of the same size used as the cathode were placed in the beaker at a spacing of 20 mm between the electrodes. A direct current (DC) potentiostat was used as the power supply for organic degradation studies with a voltage output up to 20 V.

For EC experiments, ACT (25 mg L^{-1}, 50 mg L^{-1}, 100 mg L^{-1} or 200 mg L^{-1}) and 6-CNA (50 mg L^{-1}) were placed in cells (140mL) with electrolyte (Na_2SO_4, 0.5 M), respectively. Through the experiments under different current densities, find that removal efficiency of the ACT increase was slower, and side reaction (oxygen evolution reaction) intensified, when the current density was higher than 10 mA cm^{-2}. The current density of 10 mA cm^{-2} was selected as the appropriate value. So EC experiments were performed under DC current of 0.12 A, which resulted in a current intensity of 10 mA cm^{-2}. The EC cells were placed on a magnetic stirrer for continuous mixing. Samples were withdrawn from the electrolyzed solution at a pre-determined time to analyze the model organic compounds, total organic carbon (TOC), UV absorbance, and intermediate products.

According to the related article [28], UV absorbance spectra scanning range is identified from 280 nm to 200 nm. The characteristic absorption wavelength is 245nm for water samples before and after degradation. The method of UV absorbance

spectrum was chosen to express the concentration of the ACT and the removal efficiencys of ACT and TOC of each period were expressed as the following Eq. 2.

$$\eta = \frac{C_0 - C_t}{C_0} \times 100\% \quad (2)$$

Where C_0 is the ACT concentration or the total organic carbon at the beginning, C_t is the ACT concentration or the total organic carbon at the end time of each period.

3. Results and Discussion

The preceding article [24] revealed that doping rare earth Er had effects on scanning electron microscopy (SEM, Fig. S1), X-ray diffraction (XRD, Fig. S2), and energy dispersive spectrometer (EDS, Table S1) for electrodes, details are presented in the Supplementary Information (SI).

3.1 characterization of the precursor

3.1.1 The influence of the calcination temperature

The experiments that investigated the influence of calcination temperatures (550 ℃, 600 ℃, 650 ℃, 700 ℃ and 750 ℃) on removal rate of ACT were carried out in the 0.5 M Na_2SO_4 solution with 50 mg L^{-1} ACT at room temperature. There was a space (20 mm) between these two electrodes cooperating with magnetic stir.

From Fig. 2, the EC activity of the five electrodes for ACT removal lied in the order of 650 ℃ > 600 ℃ ≈ 700 ℃ > 550 ℃ > 750 ℃. When the calcination temperature was 650 ℃, the removal efficiency reached 87.45 %. Nevertheless, when the calcination temperature increased to 750 ℃, the removal efficiency was only 63.9 %. Besides, for the solution containing 50 mg L^{-1} ACT under the same experimental conditions, the removal efficiencies for the Er doped Ti/SnO_2–Sb electrode and Ti/SnO_2–Sb electrode were 87.45% and 65.73%, respectively. The Sn/ Sb/ Er molar ratios were 100: 6: 0.5 for doping and 100: 6: 0 for undope. Doping appropriate Er could improve the EC performance of electrodes.

Some researchers [3, 4, 18] thought the main mechanism that calcination temperature affects the EC performance and stability of the electrode as follows. The suitable calcination temperature could obtain a better crystallinity of SnO_2 grain, get a higher ordered degree in the atomic lattice of SnO_2 lattice, and reduce the oxygen vacancy defect in the crystal. Therefore, these make for occurring electrochemical combustion reaction, and oxidized organic matter into CO_2 and H_2O thoroughly in a relatively short time. For the lower calcination temperature, the process of oxidation

decomposition was incomplete and the crystallinity of SnO_2 grain was poor. The EC performance of the electrode would not achieve the ideal state. If the calcination temperature is too high, the growth of SnO_2 grain accelerates that is easy for causing the secondary crystallization, making the grain distribution of coating nonuniform, and resulting in the poor density of electrode coating, which might contribute to generating the nonconductive TiO_2 in the titanium substrate. At last, these reasons were expected to result in the electrode instability and the decrease of electro-catalytic property.

In conclusion, 650 ℃ was considered as the suitable calcination temperature, Santos et al. reached similar conclusion on calcination temperature [25].

3.1.2 Analysis on phase transformation of the containing Er precursor

Fig. 3 presents the TGA-DTA spectrogram of the xerogel sample of doping Er, and the thermal oxidation process of the xerogel sample in stages.

First stage is from 38 ℃ to 305 ℃. The weight loss of the xerogel sample reaches the maximum, and the ratio of weight loss is about 75.92 %. There are three weight loss steps: (1) from 38 ℃ to 100 ℃, the volatilization of water that adsorbs and remains on the xerogel sample, shows a endothermic peak corresponding to the DTA curve. (2) from 100 ℃ to 250 ℃, the volatilization of the excess EG and the residual moisture shows a endothermic peak corresponding to the DTA curve. There is a weak exothermic peak in the DTA curve by possible reason of removing nitrate in the sample. (3) from 250 ℃ to 305 ℃, due to $-CH_2-CHOH-$ groups decomposing into -CH=CH- in the CA, the weight of sample decreases dramatically, which shows a endothermic peak.

Second stage is from 305 ℃ to 437 ℃. The weight loss of the xerogel sample is about 5.9 %, which is owing to the citric acid metal complex decomposing into metal oxides [29]. The DTA curve increases slowly accompanied with the temperature increase. The heat emission of the xerogel sample is slow, and there is not an obvious exothermic peak. The xerogel sample shifts from amorphous form to orientations form, and forms SnO_2 crystal.

Third stage is from 437 ℃ to 527 ℃. The weight loss of the xerogel sample is about 5.95 %. There is a sharp exothermic peak at 512.2 ℃ in the DTA curve corresponding to SnO_2 transforming amorphous crystalline state into quartet rutile phase crystalline state [30, 31]. Moreover, previous literature [24] also revealed SnO_2

transformed amorphous crystalline state into quartet rutile phase crystalline state by the analysis of XRD shown in Fig. S2.

Fourth stage is from 527 ℃ to 664 ℃. There are two weak exothermic peaks in the DTA curve at 578.10 ℃ and 616.73 ℃. The peaks indicate oxidation of Sb_2O_3 form Sb_2O_4, which is consisted of Sb_2O_3 and Sb_2O_5. The volatilization of Sb_2O_3 at high temperature causes 5.21 % weight loss.

Fifth stage is from 664 ℃ to 700 ℃. The weight of sample does not change any longer and. There is a weak exothermic peak in the DTA curve at 681.02 ℃. The weak exothermic peak indicates Sb_2O_4 that is oblique square cervantite type [32], form at 681.02 ℃.

In addition, the TGA-DTA spectrogram of the xerogel sample without Er doping is generally similar with that of the doped sample as shown in the Fig. S11. However, from 100 ℃ to 250 ℃, the volatilization of the excess EG and the residual moisture shows a smaller endothermic peak and less ratio of weight loss (68.02%) compared with the TGA-DTA spectrogram of the xerogel sample of doping Er at the first stage, possibly due to the lack of nitrate.

According to the above analysis and the TGA-DTA spectra, minimum forming temperature of SnO_2 (quartet rutile phase crystalline state) is about 550 ℃, so the thermal oxidation temperature should be higher than it in electrode preparation process, which is in agreement with 3.1.1 chapter's conclusion.

3.1.3 UV/Vis/NIR diffuse reflectance spectra analysis

Fig. 4 gives the UV/Vis/NIR diffuse reflectance spectra of precursor powders and the illustration is amplification of spectra at 230 nm - 400 nm. After the Er was doped into the precursor powder, optical absorption peaks of the sample moved to short-wave direction slightly. The phenomenon of the blue shift in absorption peak could be attributed to the quantum size effect [33]. According to the Burstei-Moss mobility theory, the blue shift in the absorption peak indicates that the precursor powder with Er has a higher carrier concentration, signifying the Er doped Ti/SnO_2-Sb electrode has better electrical conductivity than the Ti/SnO_2-Sb electrode. The improving electrical conductivity could enhance current efficiency and increase efficiency of electro-catalysis.

The band gap energy of semiconductors (E_g) can be estimated from the absorption edge (λ_g) using formula [34]:

$$Eg = 1240/\lambda_g \quad (3)$$

λ_g of prepared electrodes and corresponding E_g calculated by Eq. 3 are shown in Fig. S9 and Table 1, respectively. The doping of Sb and Er into SnO_2 transformed the band gap of SnO_2 semiconductor structure.

Sb^{5+} doped in the SnO_2 increased the concentration of electrons in the conduction band and facilitates conductivity. Hence, the band gap energy value of SnO_2-Sb electrode reduced to 3.31 eV. Er^{3+} doped in the SnO_2-Sb is beneficial to electronic transfer from valence band to conduction band, and the band gap energy value of 0.5 mol% Er doped in the SnO_2-Sb reduced to 3.14 eV. As presented in Fig. 3, a blue-shift in absorbance peak was observed in our experiment. But for SnO_2, the band gap energy value is 3.8 eV [35, 36], which is significantly more than the calculated value of samples.

Narrower band gap may lead to higher carrier concentration, which can improve electrical conductivity of electrodes [37]. The band gap of Er doped in the Ti/SnO_2-Sb is lower than the band gap of 0 mol% Er doped in the Ti/SnO_2-Sb, resulting in better electrical conductivity of electrodes.

3.2 Electrochemistry characterization of the electrode

3.2.1 Examination of electrode by linear sweep voltammetry

The linear sweep voltammograms (LSVs) of the electrodes in the 0.5 M Na_2SO_4 are given in Fig. 5. For the two kinds of electrodes that are the Er doped Ti/SnO_2-Sb electrode and the Ti/SnO_2-Sb electrode, the initiation potentials for oxygen evolution were around 1.85 V and 1.6 V (vs. SCE), respectively, the absolute value of oxygen evolution was generally consist with previous literature [38]. Adding the rare earth Er into electrode can improve the initiation potential of the electron's oxygen evolution. In wastewater treatment, higher oxygen evolution voltage was suggested more desirable [39]. The lower oxygen evolution voltage has the disadvantage on degrading organics in aqueous electrolyte, because anodic oxygen evolution belongs to the side effect, causes an unwanted power loss and consumes active substances.

3.2.2 The oxygen evolution reaction kinetic analysis

According to the high overpotential regions in the Fig. 5 and Eq 1, we calculated the oxygen evolution reaction kinetic parameters (Table 2) of different electrodes and obtain Tafel plots shown in Fig. 6.

In Eq. 1, "a", the overpotential value under unit of the current density, represents the intercept value obtained with Origin and contrasts the difficulty level of electron

transfer in different electrode systems, and "b" (Tafel slope) reflects the electrode potential changes speed. In general, Tafel analysis presents the information of exchange current density and over-potentials [40-42]. High exchange current density and low Tafel slope are considered to be beneficial to OER [43]. In this case that the Tafel slope is higher, the oxygen evolution reaction is easier on account of the smaller polarization resistance. From Fig. 6 and Table 2, there is a nice linear relation between electrode potentials and current densities logarithm, which meets the Eq. 1. The value of "a" for the Er doped Ti/SnO_2-Sb electrode is larger than the value of "a" for the Ti/SnO_2-Sb electrode, and the former Tafel slope value is less than the latter. This indicates that adding the proper amount of rare earth Er into electrode can improve the electron transfer rate, reduce the energy loss in the process of wastewater treatment, and improve current efficiency.

3.2.3 Examination of electrode by cyclic voltammetry

It is generally believed that organic compounds in aqueous solutions can be oxidised on an anode by direct electron-oxidation and indirect electron-oxidation [14, 16, 44, 45]. In the direct electron-oxidation process, organic compounds are adsorbed on the anode surface and transfer electrons to the anode. In the indirect electron-oxidation process, it is generally considered that oxygen containing radicals, especially the hydroxyl radicals generated from water electrolysis, play a critical role in the EC oxidation mechanism of organic substances [45-47], Fig. 7 shows cyclic voltammograms (CVs) in the 0.5 M Na_2SO_4 with and without 25 mg L^{-1} ACT. In Fig. 7, we can see that there are no anodic peaks in the two types of aqueous solutions before the oxygen evolution potentials and adding the ACT has no obvious effect on CVs. It indicates that the ACT of solution don't happen the direct electron transfer reaction in the self-made electrode, and the process of ACT degradation is "indirect electron-oxidation" rather than "direct electron-oxidation" [45, 48].

3.2.4 Examination for the service life of electrode

The electrodes should not only have higher electrochemical activity but good stability. The small current density in actual application required a considerable long time of the examination for the service life of electrode. Taking this factor into consideration, we used the method of accelerated test to measure the service life, and predicted the actual working life of the electrodes by Eq. 4:

$$\tau_2 = \tau_1 \left(\frac{i_1}{i_2} \right)^2 \quad (4)$$

Where τ_2 and τ_1 are actual working life and accelerated service life, i_2 and i_1 are actual working current density and accelerated current density, respectively.

The method of accelerated test of service life for Er doped Ti/SnO_2–Sb electrode was similar with previous literature [11]: The distance between the tested electrodes (anode) and Ti plate (cathode) was 20 mm, and an external DC power source provided the current density of 2000 A m^{-2} in electrolysis cells with 1.0 mol L^{-1} H_2SO_4 as electrolyte. The accelerated service life test of electrode would be end up with 5 V increasing of electrolysis cells voltage.

The results of tested accelerated service lives of Er doped Ti/SnO_2–Sb and Ti/SnO_2–Sb electrode were shown in Table. 3. The actual working lives of electrodes were calculated by Eq. 4. The actual working life of Er doped Ti/SnO_2–Sb electrode was obviously longer than that of Ti/SnO_2–Sb electrode, which would reduce the cost of electrochemical degradation in actual processes.

Besides, Fig.S1(a) and (b) showed the morphologies of freshly prepared 0 mol% Er doped and 0.5 mol% Er doped Ti/SnO_2-Sb electrode ,respectively. Cracked-clay morphology existed for both kinds of electrode surface coatings. Compared with undoped samples, the crack of doped samples was narrower, more compact, and existed more refined grains, which were beneficial to improving the stability of the electrodes, increasing the specific surface area, and extending the life of the electrodes [24].

3.4 Performance of the electrode on ACT degradation

The electrode degrades organic matter mostly associating with the oxygen evolution reaction, so it is important to research the oxygen evolution reaction. The oxygen evolution reaction of the Ti/SnO_2-Sb electrode is generally divided into the following steps [4, 49]:

$$SnO_{2-x} + H_2O \rightarrow SnO_{2-x}(HO\cdot) + H^+ + e^- \quad (5)$$

$$SnO_{2-x}(HO\cdot) \rightarrow SnO_{2-x+y} + yH^+ + ye^- \quad (6)$$

$$SnO_{2-x+y} \rightarrow SnO_{2-x} + \frac{1}{2} yO_2 \quad (7)$$

$$SnO_{2-x}(HO\cdot) \rightarrow SnO_{2-x} + \frac{1}{2} O_2 + H^+ + e^- \quad (8)$$

As Eq. 5 shows, water molecule is oxidized on the electrode surface and forms adsorption state of hydroxyl radical that is $SnO_{(2-x)}(HO\cdot)$. On account of existing the oxygen vacancy in the SnO_2 grain, $SnO_{(2-x)}(HO\cdot)$ might either come up the oxygen evolution reaction as Eq. 8, or come about the oxygen atom transfer reaction developing the high valence state oxide ($SnO_{(2-x+y)}$, Eq. 6), further occur the oxygen evolution reaction as Eq. 7. The oxygen content of $SnO_{(2-x+y)}$ is always less than 2 (i.e., 2-x-y＜2). Besides, the reaction system was under an acidic environment, the changes of pH with various electrolysis time were shown in Fig. S4. The FT-IR analysis also supported the above formula in Fig. S3.

In the EC system, degradation organic matter also needs $SnO_{(2-x)}(HO\cdot)$ as the main participator (Eq. 9) [3].

$$Organics + SnO_{2-x}(HO\cdot) \rightarrow CO_2 + SnO_{2-x} + zH^+ + ze^- \quad 9$$

Based on the CVs analysis result that the process of ACT degradation is "indirect electron-oxidation", adsorption state $SnO_{(2-x)}(HO\cdot)$ on the electrode surface should react with the ACT spreading to near the electrode surface. Some are mineralized into small molecule inorganic, the others are degraded to organic intermediates firstly and small molecule inorganics gradually (Eq. 10).

$$ACT_{ads} \xrightarrow{SnO_{2-x}(HO\cdot)} Intermediate_{ads} \xrightarrow{SnO_{2-x}(HO\cdot)} CO_2 + H_2O + Others \quad 10$$

With constant current (10mA cm^{-2}), the presence of hydroxyl radicals played an important role in the degradation process, as shown in Fig. S6. The degradation rate " r " for the ACT would be expressed as Eq. 11.

$$r = \frac{d[ACT]}{dt} = k_{ACT}[HO\cdot]^{\alpha}(ACT)^{\beta} = k_{app(ACT)}(ACT)^{\beta} \quad 11$$

Where k_{ACT} is the real rate constant. $k_{app\ (ACT)}$ is the apparent rate constant of the ACT oxidation. α and β are the reaction order relating to HO• and ACT, respectively.

Then we changed the initial concentrations of ACT (25 mg L^{-1}, 50 mg L^{-1}, 100 mg L^{-1}, 200 mg L^{-1}) with other conditions unchanged, and discussed the degradation kinetics. We processed experimental data and obtain relation between ln (ACT_0/ACT_t) and various time plots shown in Fig. 8. The straight lines obtained in Fig. 8 suggest that the kinetics of ACT degradation is in line with the pseudo-first order reaction kinetics. So, Eq. 11 could be rewritten as Eq. 12 and Eq. 13. Additionally, ACT concentration can be obtained from the curve of calibrated absorbency value vs. concentration of ACT at 245nm shown in Fig. S5.

$$r = \frac{d[ACT]}{dt} = k_{app(ACT)}(ACT) \quad 12$$

$$ln\frac{(ACT_0)}{(ACT_t)} = k_{app(ACT)}t = k_m \frac{S}{V} t \quad 13$$

Where k_m is the apparent mass transfer coefficient. S is the effective electrolysis area and V is the volume of the electrolyte.

Table 4 summarizes the removal amount of ACT after 180 min electrolysis and the degradation kinetic parameters for different initial ACT concentrations.

Table 4 reflects that the mass transport rate ($k_{m\ (ACT)}$) that stands for ACT molecule diffusion from the solution to the surface of electrode, was always varying with the increase of ACT initial concentration. The higher the initial concentration of ACT, the more removal amount of ACT after 180min electrolysis.

Table 4 also shows that the apparent mass transfer coefficient (k_m) and apparent rate constant ($k_{app\ (ACT)}$) decreased with the increase concentration of ACT that ranged from 25 mg L^{-1} to 200 mg L^{-1}. k_m and $k_{app(ACT)}$ changed little in the low concentration region, but in high concentration region varied tremendously. The reason for causing these might be as follow.

The values of k_m or $k_{app(ACT)}$ should be very close in theory at different concentrations. However, hydroxyl radicals (HO·) concentration should be regarded as invariant at constant current (10 mA cm^{-2}). According to Eq. 10, degradation generated some intermediate and conducted the oxygen evolution reaction. If increasing amount of ACT in aqueous solution, intermediate is accumulated accompanying with the degradation process. Nevertheless, HO· has a strong ability of oxidation and reacts with most organic matters, intermediate competes with ACT molecule for HO·. So the parameters are lower gradually and HO· is another important factor for the ACT degradation.

3.5 ACT degradation and TOC removal

In the electrochemical oxidation of ACT (50 mg L^{-1}), the concentration of ACT after different periods of galvanostatic electrolysis was analyzed by UV-spectrometer and TOC analyses. Eq. 2 was applying for the removal efficiencies of ACT and TOC. With the time increasing, the removal efficiencies of ACT and TOC were also increasing progressively. After 180 min electrolysis, the ultimate removal efficiencies are 87.45 % (ACT removal) and 69.31 % (TOC removal). So the Er doped Ti/SnO_2-Sb electrode is effective for ACT mineralization shown in Fig. 9.

However, the TOC removal efficiency is less than the ACT removal efficiency all the time. Some articles also expressed the similar phenomenon in the anode electrolysis of refractory wastewaters [4, 50]. This indicates that the formation and accumulation of some organic intermediates (such as 6-CNA) may prolong electrolytic time, before ACT was thoroughly decomposed into inorganic substances, such as carbon dioxide, water molecule.

Fig. 10 Linear regression for ln (TOC_0/TOC_t) as a function of time at the current density of 10 mA cm^{-2}.

Handling the TOC removal data got relation between ln (TOC_0/TOC_t) and various time plot and generated straight line (Fig. 10), illustrating that the reaction kinetic of TOC removal matched the pseudo first-order kinetics expressed as the following equation.

$$ln \frac{TOC_0}{TOC_t} = kt \qquad 14$$

Where TOC_0 is the total organic carbon at the beginning, TOC_t is the total organic carbon at the end time of each period.

3.6 Degradation pathway and mechanism analysis of ACT

The UV spectrum is often applied to analyze compound containing a conjugated system. Molecular structures of compounds and energy level gap of electronic transition are different, so the wavelength of maximum absorption (λ_{max}) is distinct for different compounds. According to the organic spectral theory, condition that the organics produce UV absorption includes chromophore and auxochrome. The chromophore is general the group containing π electron, such as:

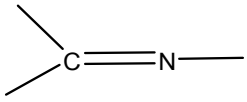

imine

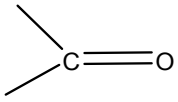

carbonyl

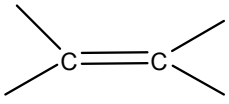

olefins

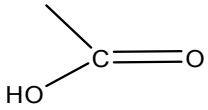

carboxyl

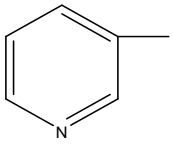

pyridyl

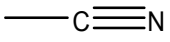

cyano

The auxochrome is common the group containing n electron, like $-OH$, $-NH-$, $-Cl$, $-NR_2$ and so on. Itself has no UV absorption, nevertheless often affect the $\lambda_{max,}$ when connecting with the chromophore. There are three main UV absorption bands for the organic matters, namely the R band, K band and B band, whose characters were listed in Table 5.

The UV scan curves of electrolytes (50 mg L^{-1} ACT, 50 mg L^{-1} 6-CNA) at some electrolysis time with the Er doped Ti/SnO_2-Sb electrode, were illustrated in Fig. 11A and Fig. 11B, respectively.

As Fig. 11A displayed, the peak of wavelength absorption is always at 245 nm, indicating the presence of the K band [28, 58] before and after ACT degradation. Because the molecular structure of ACT contains chromophores (imine, amino and pyridyl) and auxochromes (-*Cl*, -CH_3, -NR_2), K band was formed by the conjugated double bond absorption which consists of imine and amino. During the electrolysis, the peak wavelength absorption is decreasing, suggesting conjugated double bond have been destroyed little by little. Furthermore, there were two new absorption peaks in 275 nm and 265 nm after 120 min electrolysis, indicating the presence of intermediate products containing a pyridine ring. Castan et al. and Gipson et al. obtained similar conclusions in previous studies [51, 52]. The two new absorption peaks corresponded to R band and B band of pyridine ring, respectively. Pyridine ring connected with auxochrome, i.e., hydrogen bonded at pyridine nitrogen and carbonyl group [53], promoted absorption band shifting to red shift. The two new absorption peaks in 275 nm and 265 nm continuously decreased, illustrating the destruction of pyridine rings in the intermediate products.

There are three absorption peaks in 224 nm, 265 nm and 275 nm corresponding to the K band, B band and R band, respectively (Fig. 11B). Strong absorption in the K band was formed by conjugated system that is made up by pyridine ring and carboxyl. After 180min electrolysis, the three characteristic absorption peaks are almost disappearing. These further proved that organic matter containing pyridine ring occurs ring-opening reaction in EC system.

Mass spectrograms of the ACT before and after treatment were exhibited in Fig. 12, and Table 6 listed possibly stable degradation products. Based on the above consequence, a degradation pathway was proposed for the ACT EC as shown in Fig. 13. Some undetected compounds were also written out in brackets of Fig. 13 and

could readily and rapidly be oxidized or hydrolyzed to other or small inorganic molecules.

Because the ACT wastewater has the characteristic of low alkalinity, ACT proceeded the deprotonation reaction in oxidation system, in which HO· is the main active substance, and active site of the ACT molecule is α-C in tertiary amine. HO· captures hydrion (H^+) from α-C, generating water molecule (H_2O) and α-amido hydroxyl radical ($-HC^{\bullet}-N<$).α-amido hydroxyl radical has the high reducibility [54], so oxygen molecule (O_2) was reduced to superoxide radical (O_2^-) [55]and it was oxidized to organic 1.

The superoxide radical (O_2^-) continues to react based on Eq 15 and 16 and form oxygen molecule (O_2) and hydrogen peroxide (H_2O_2) [56.]. Minghua Zhou [57] verified that there was no H_2O_2 molecule in the EC degradation of phenol with anode. Therefore, there was a relationship between H_2O_2 of in-situ reaction with special structure of ACT in the study.

$$O_2^- \cdot + H^+ \Leftrightarrow HO_2 \cdot \quad 15$$

$$2HO_2 \cdot \rightarrow H_2O_2 + O_2 \quad 16$$

According to deprotonation reaction mentioned above, organic 1 was further oxidized and generated organic 3 and 4 in Fig.13. The pathway is consistent with Maria L. Dell'Arciprete [19] proposed, who employed photocatalytic degradation of the ACT.

Mass spectrum test detected three molecular ion peaks, namely m/z=164.9198, 146.9768 and 144.9805 representing organic 5, 6 and 8. Verify whether if 6-CNA as an intermediate product was oxidized further and generated three organics, so EC experiment that took 6-CNA as a model organic compound, was conducted under the same conditions as ACT. Mass spectrograms of the 6-CNA before and after treatment were displayed in Fig. 14.

As Fig. 14b shows, there are three molecular ion peaks as similar to the aforesaid in mass spectrogram of 6-CNA after degradation, deducing that three organics were generated by 6-CNA reacting with HO· during the EC degradation of ACT.

The hydroxyl radical (HO·) has a close electrical characteristic, and tends to attack the position, whose electron cloud is denser than the other in the molecular structure. Pyridine ring is similar to benzene ring. The p-orbital in each atom is perpendicular to the ring plane, these p-orbitals parallel to each other and the sides

overlap to form a closed π bond. There is a hybrid orbital sp2 for N atom on pyridine ring. It doesn't participate in bonding and exists in form of lone electron pair that skews π electron cloud to the N atom forming a high density of electron cloud around the N atom, so the density of electron cloud is lower for the rest of the ring. The N atom was attacked by HO· in the pyridine ring of the 6-chloronicotinic acid and is separated from the pyridine ring in form of NO_2^- or NO_3^-. Unpaired electrons of two C atoms beside the N atom attract each other forming a new key (organic 5).Reduction of organic 5 occurred electrophilic addition reaction generating organic 6 by in-situ reaction's H_2O_2. Active Cl atom and double bond that are easy to develop an electrophilic addition reaction, is replaced by HO· and reduced to single bond by H_2O_2, respectively (organic 7). Besides, previous literature [58] about acetamiprid removal by the low-temperature plasma using dielectric barrier discharge could also achieve similar conclusion, which 6-chloronicotinic acid was reduced to piperidine derivative. The above degradation reactions were also mentioned by electro-catalytic degradation mechanism of nitenpyram using Ti-based SnO_2–Sb [59] of our previous study.

Organic 7 (cyclopentane carboxylic acid), organic 8 (piperidine derivative) and amide derivative that was generated by oxidized organic 4, had well biodegradable property, further were oxidized to low molecular weight organic matters and inorganic matters by HO·.

4. Conclusions

Adding rare earth Er into Ti/SnO_2-Sb electrode could improve the electrical conductivity and oxygen evolution potential of the electrode. The electrode had a nice EC performance for degradation of ACT at 650 □ chosen as the suitable calcination temperature. The removal efficiency of ACT and TOC reached 87.45 % and 69.31 % after 180 min electrolysis for synthetic wastewater containing 50 mg L^{-1} ACT at the current density of 10 mA cm^{-2}. The kinetics of ACT and TOC by electro-catalysis was in accordance with pseudo-first order reaction kinetics. According to the UV spectrograms and mass spectrograms, a degradation pathway was proposed for ACT. 6-CNA was identified as the main intermediate product before the pyridine ring cleavage, finally converted to small molecules. The degradation mechanism involved the attack of HO· and H_2O_2.

On the whole, EC appeared a higher removal efficiency for the ACT, and could

be an attractive alternative for pre-treatment or treatment of wastewater containing ACT.

Acknowledgements

The research was supported by Technological Progress Plan of Shandong, grant No. 2011GGE27048, China.

References

[1] C. Comninellis, Electrochim. Acta., 1994, 39, 1857.

[2] C. Comninellis, C. Pulgarin, J. Appl. Electrochem., 1991, 21, 703.

[3] Y. J. Feng, Y. H. Cui, B. Logan, Z. Q. Liu, Chemosphere, 2008, 70, 1629.

[4] X.Y. Li, Y. H. Cui, Y. J. Feng, Z. M. Xie, J. D. Gu, Water Res., 2005, 39, 1972.

[5] J. T. Kong, S. Y. Shi, L. C. Kong, X. P. Zhu, J. R. Ni, Electrochim. Acta., 2007, 53, 2048.

[6] M. Panizza, G. Cerisola, Env. Sci. Technol., 2004, 38, 5470.

[7] B. O. Park, C. D. Lokhande, H. S. Park, et al. Mater. Chem. Phys., 2004, 87, 59-66.

[8] J. M. Hu, J. Q. Zhang, C. N. Cao, Int. J. Hydrogen Energy, 2004, 29, 791-797

[9] J. B. Cheng, H. M. Zhang, G. B. Chen, Y. N. Zhang, Electrochim. Acta., 2009, 54, 6250.

[10] A. T. Marshall, R. G. Haverkamp, Electrochim. Acta., 2010, 55, 1978.

[11] B. Correalozano, C. Comninellis, A. D. Battisti, J. Appl. Electrochem., 1997, 27, 970.

[12] D. Devilliers, M. T. Dinh-Thi, E. Mahe, Q. L. Xuan, Electrochim. Acta., 2003,48, 4301.

[13] Y. Mohd, D. Pletcher, J. Electrochem. Soc., 2005, 152, 97.

[14] J. D. Rodgers, W. J. Jedral, N. J. Bunce, Environ. Sci. Technol., 1999, 33, 1453.

[15] E. C. P. E. Rodrigues, P. Olivi, J. Phys. Chem. Solids, 2003, 67, 1105.

[16] A. M. Polcaro, S. Palmas, F. Renoldi, M. Mascia, J. Appl. Electrochem., 1999, 29, 147.

[17] S. P. Li, H. B. Wang, J. F. Lian, X. Y. Zeng, Adv. Mater. Res., 2012, 455, 1356.

[18] Y. J. Feng, Y. H. Cui, J. Hazard. Mater., 2010, 178, 29.

[19] M. L. Dell'Arciprete, L. Santos-Juanes, A. A. Sanz, R. Vicente, A. M. Amat, J. P. Furlong, D. O. Mártire, M. C. Gonzalez, Photochem. Photobilo. Sci., 2009, 8, 1016.

[20] O. Malev, R. S. Klobučar, E. Fabbretti, et al., Pestic. Biochem. Phys., 2012, 104, 178-186.

[21] P. N. Moza, K. Huster, E. Feicht, A. Kettruo, Chemosphere, 1998, 36, 497.

[22] S. Malato, J. Caceres, A. Agüera, M. Mezcua, D. Hernando, J. Vial, A. R. Fernández-Alba, Environ. Sci. Technol., 2001, 35, 4359.

[23] G. Mailhota, M. Sarakhaa, B. Lavedrinea, J. Cáceresb, S. Malatob, Chemosphere, 2002, 49, 525.

[24] S. P. Li, X. Y. Zeng, Y. Y. Jiang, Adv. Mater. Res., 2013, 699, 724.

[25] I. D. Santos, S. R. Gabriel, J. C. Afonso, A. J. B. Dutra, Mater. Res., 2011, 14, 408.

[26] E. Gileadi, E. K. Eisner, Corros. Sci., 2005, 47, 3068.

[27] N. W. Fan, Z. K. Li, L. Zhao, N. M. Wu, T. Zhou, Chem. Eng. J., 2013, 214, 83.

[28] J. V. Guzsvány, J. J. Csanádi, S. D. Lazić, F. F. Gaál, J. Braz. Chem. Soc., 2009, 20, 152.

[29] M. Alves, S. Souza, M. Silva, et al., J therm. Anal. Calorim., 2009, 97, 179-183.

[30] K. N. P. Kumar, J. Kumar, K. Keizer, J. Am. Ceram. Soc., 1994, 77, 1396-1400

[31] K. N. P. Kumar, K. Keizer, A. J. Burggraaf, et al., Nature, 1992, 358, 48-51.

[32] Z. H. Liang, Y. F. Sun, Y. B. Ding, W. T. Zhang, Rare. Metal. Mat. Eng., 2011, 40, 64.

[33] J. Woltersdorf, A. S. Nepijko, E. Pippel, Surf. Sci., 1981, 106, 164.

[34] J. Fu, B. Chang, Y. Tian, et al., J. Mater. Chem. A, 2013, 1, 3083-3090.

[35] A. Hagfeldt, M. Graetzel, Chem. Rev., 1995, 95, 49-68.

[36] Y. Yamashita, K. Yoshida, M. Kakihana, et al., Chem. Mater., 1999, 11, 61-66.

[37] R. Kötz, S. Stucki, B. Carcer, J. App. Electrochem., 1991, 21, 14-20.

[38] H. Xu, A. P. Li, Q. Qi, et al., Korean J. Chem. Eng., 2012, 29, 1178-1186.

[39] R. Kötz, S. Stucki, B. Carcer, J. App. Electrochem., 1991, 21, 14-20.

[40] L. M. Da Silva, J. F. C. Boodts, L. A. D. Faria, Electrochim. Acta., 2001, 46, 1369-1375.

[41] P. Shrivastava, M. S. Moats, J. Appl. Electrochem., 2009, 39, 107-116.

[42] G. N. Martelli, R. Ornelas, G. Faita, Electrochim. Acta., 1994, 39, 1551-1558.

[43] Y. Lai, Y. Li, L. Jiang, et al., J. Electroanal. Chem., 2012, 671, 16-23.

[44] L. C. Chiang, J. E. Chang, T. C. Wen, Water Res. 1995, 29, 671-678.

[45] J. Iniesta, P. A. Michaud, M. Panizza, G. Cerisola, A. Aldaz, Electrochim. Acta., 2001, 46, 3573.

[46] X.Y. Li, F. Ding, P. S. Y. Lo, S. H. P. Sin, J. Environ. Eng. ASCE, 2002, 128, 697-704.

[47] O. Simod, V. Schaller, C. Comninellis, Electrochim. Acta., 1997, 42, 2009-2012.

[45] J. Iniesta, P. A. Michaud, M. Panizza, G. Cerisola, A. Aldaz, Electrochim. Acta., 2001, 46, 3573.

[48] Y. H. Cui, Y. J. Feng, Z. Q. Liu, Electrochim. Acta., 2009 ,54, 4903.

[49] Y. Q. Wang, B. Gu, W. L. Xu, J. Hazard. Mater., 2009, 162, 1159.

[50] G. Rodrigues de Oliveiraa, N. Suely Fernandesa, J. Vieira de Meloa, D. Ribeiro da Silva a, C. Urgegheb, C. A. Martínez-Huitlea, Chem. Eng. J., 2011,168, 208.

[51] P. Castan, F. Dahan, S. Wimmer, et al., J. Chem. Soc., Dalton Trans., 1990, 9, 2679-2683.

[52] K. Gipson, B. Ellerbrock, K. Stevens, et al., J. Nanotechnolo., 2011, 2011.

[53] M. K. Nayak, S. K. Dogra, J. Mol. Struct., 2004, 702, 85-94.

[54] K. O. Hiller, K. D. Asmus, J. Phys. Chem., 1983, 87, 3682.

[55] C. V. Sonntag, H. Schuchmann, Angew. Chem. Int. Edit, 2001, 30, 1229.

[56] M. C. Gonzalez, E. Oliveros, M. W. Orner, A. M. Braun, J. Photochem. Photobiol., 2004, 5, 225.

[57] M. H. Zhou, Q. Z. Dai, L. C. Lei, C. A. Ma, D. H. Wang, Environ. Sci. Technol., 2005, 39, 363.

[58] S. P. Li, X. L. Ma, Y. Jiang, et al., Ecotox. Environ. Safe., 2014, 106, 146-153.

[59] S. P. Li, W. R. Wang, X. Y. Zeng, et al. Desalin Water Treat, 2015, 54, 1925-1938.

List Of Table and Figure Captions

Fig.1 (A) The chemical structure of ACT; (B) The chemical structure of 6-CNA.

Fig. 2 The impacts of calcination temperatures on removal efficiencies of ACT for the Er doped and undoped SnO_2-Sb electrodes.

Fig. 3 TGA-DTA spectra of xerogel sample of doping Er.

Fig. 4 UV/Vis/NIR diffuse reflectance spectra obtained from the precursor powders with and without Er for the electrodes preparation.

Fig. 5 LSVs of the Er doped and undoped SnO_2-Sb electrodes in the 0.5 M Na_2SO_4 at a scan rate of 20 mV s^{-1}.

Fig. 6 Tafel plot of different electrodes at the high overpotential regions.

Fig. 7 CVs of the Er doped SnO_2-Sb electrode in the 0.5 M Na_2SO_4 and 0.5 M Na_2SO_4 as containing 25 mg L^{-1}ACT at a scan rate of 50 mV s^{-1}.

Fig. 8 Linear regression for ln (ACT_0/ACT_t) as a function of time at the room temperature with the current density of 10 mA cm^{-2}.

Fig. 9 ACT and TOC removal efficiencies for 50 mg L^{-1}ACT by the Er doped Ti/SnO_2-Sb electrode at current density of 10 mA cm^{-2}during variation time.

Fig. 10 Linear regression for ln (TOC_0/TOC_t) as a function of time at the current density of 10 mA cm^{-2}.

Fig. 11 UV scan curves of electrolytes for: (A) ACT (50 mg L^{-1}); (B) 6-CNA (50 mg L^{-1}). The samples were diluted 10 times before measuring.

Fig. 12 (A) MS spectrograms of ACT before treatment in positive ion mode, MS range: 120-400. (B) MS spectrograms of ACT after treatment 90 min in negative ion mode, MS range: 60-420. (C) MS spectrograms of ACT after treatment 90 min in positive ion mode, MS range: 110-250. (D) MS spectrograms of ACT after treatment 90 min in positive ion mode, MS range: 136-174. (E) MS spectrograms of ACT after treatment 180 min in positive ion mode. MS condition: drying temperature: 350 ℃; sheath gas: 40; attach gas: 10; purge gas: 0; MS range: 50-800.

Table 1 Band gap energies for the Er doped and undoped SnO_2-Sb samples

Table 2 The oxygen evolution reaction kinetic parameters of different electrodes

Table 3 Service life in the accelerated test for different electrodes

Table 4 The removal amount of ACT and degradation kinetic parameters including

(A)

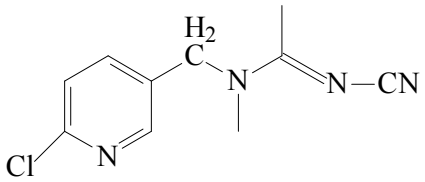

(B)

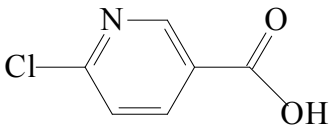

Fig.1

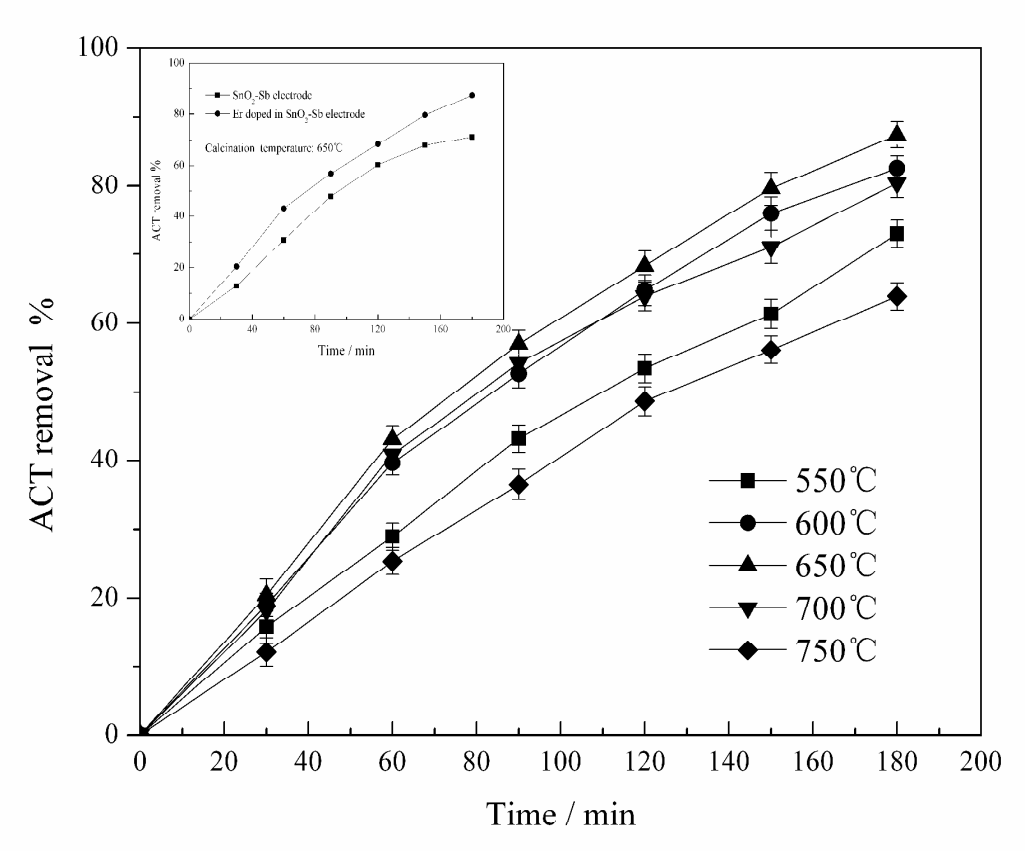

Fig. 2

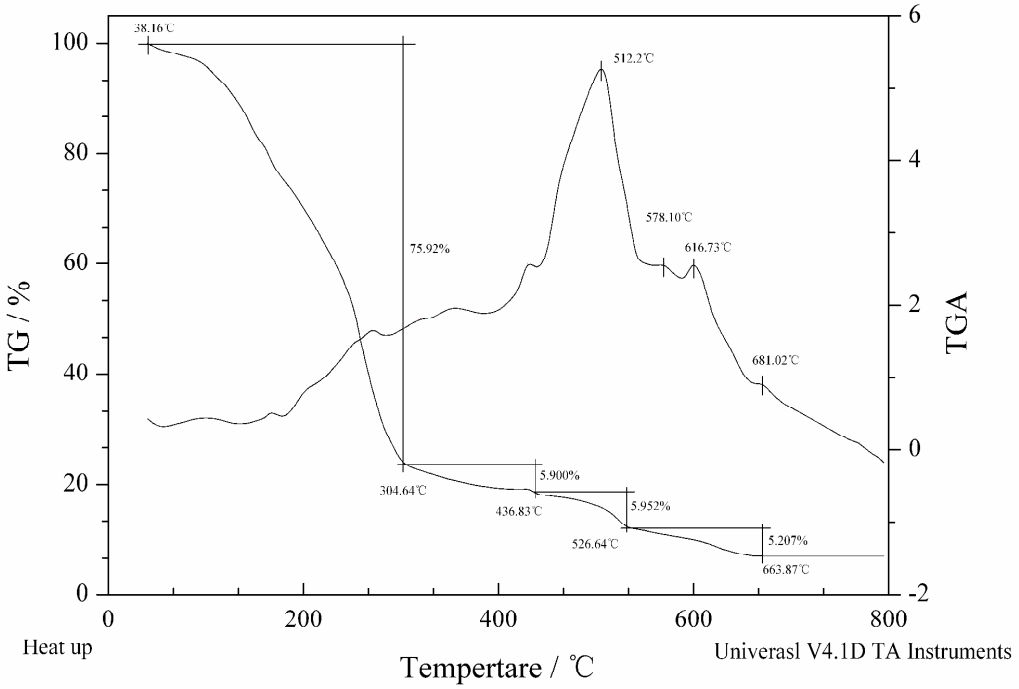

Fig. 3

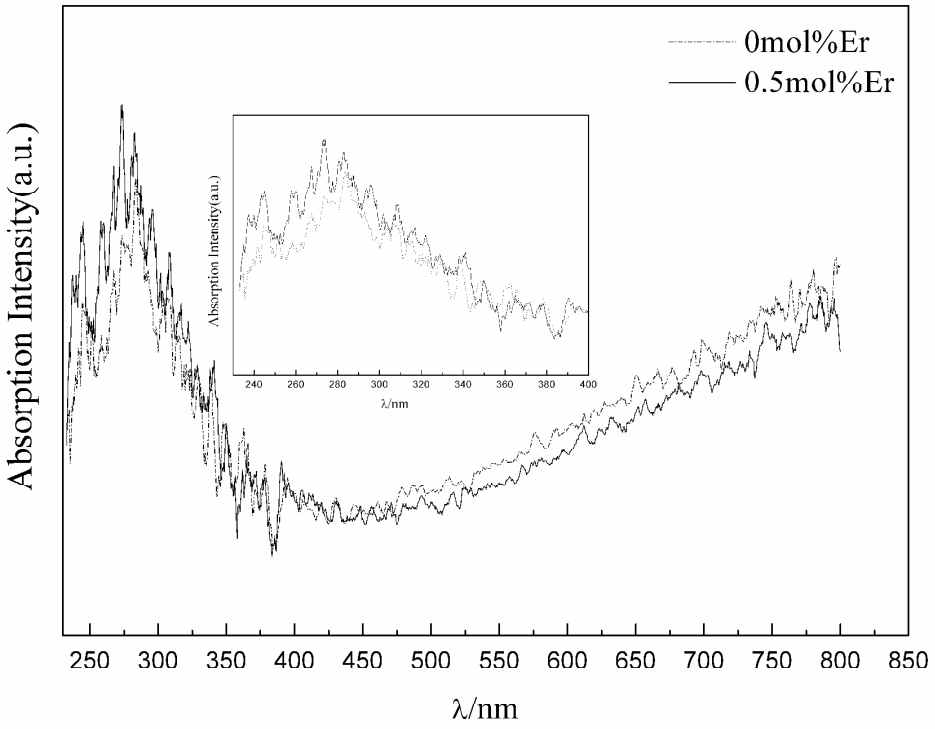

Fig. 4

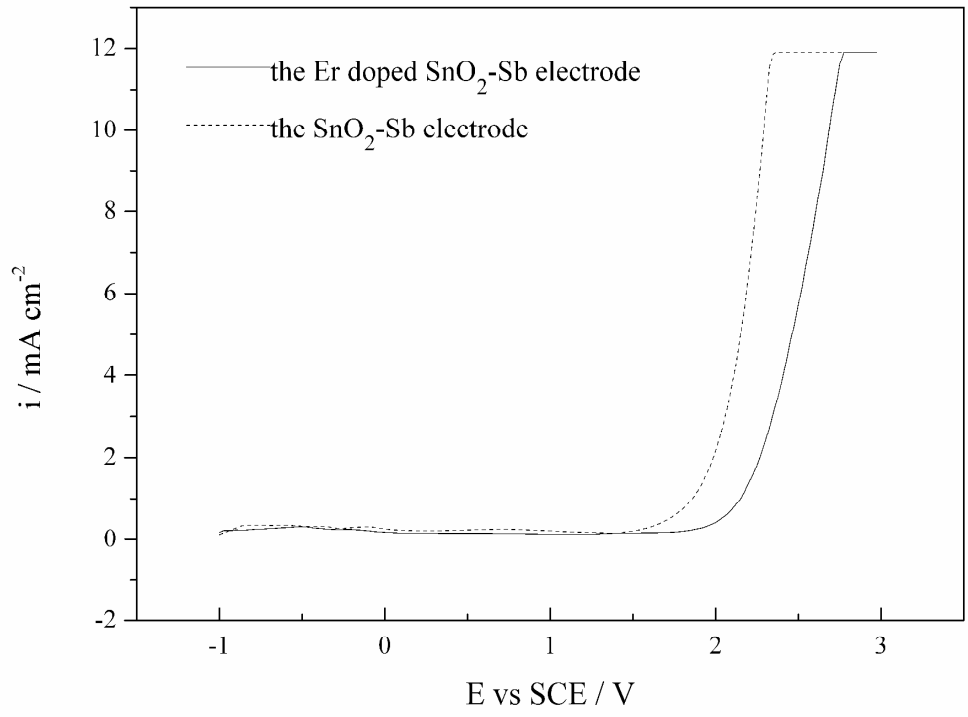

Fig. 5

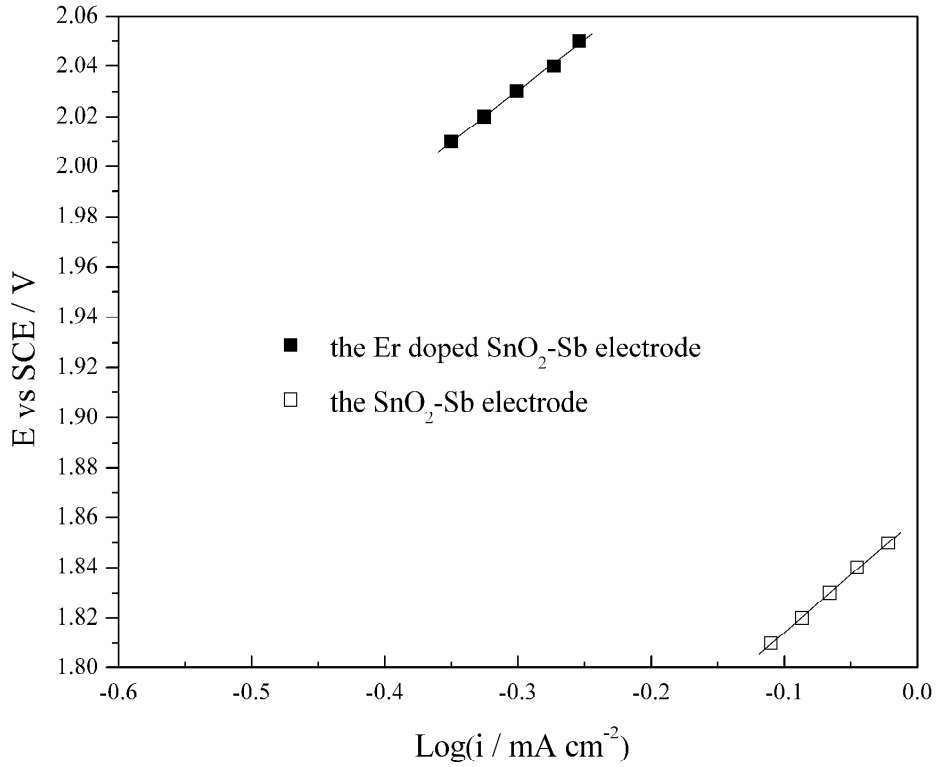

Fig. 6

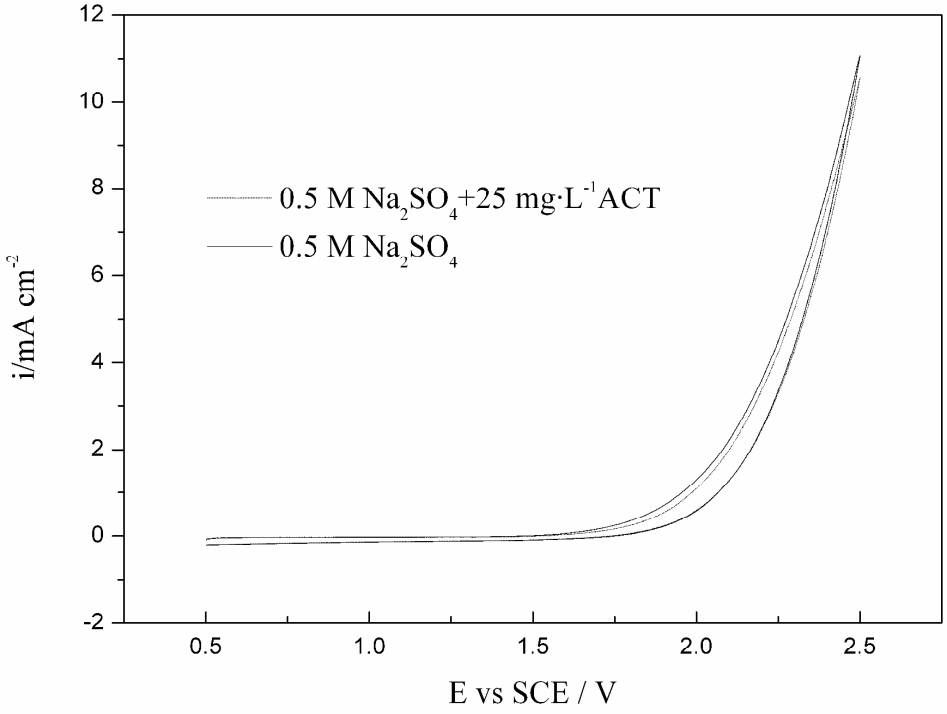

Fig. 7

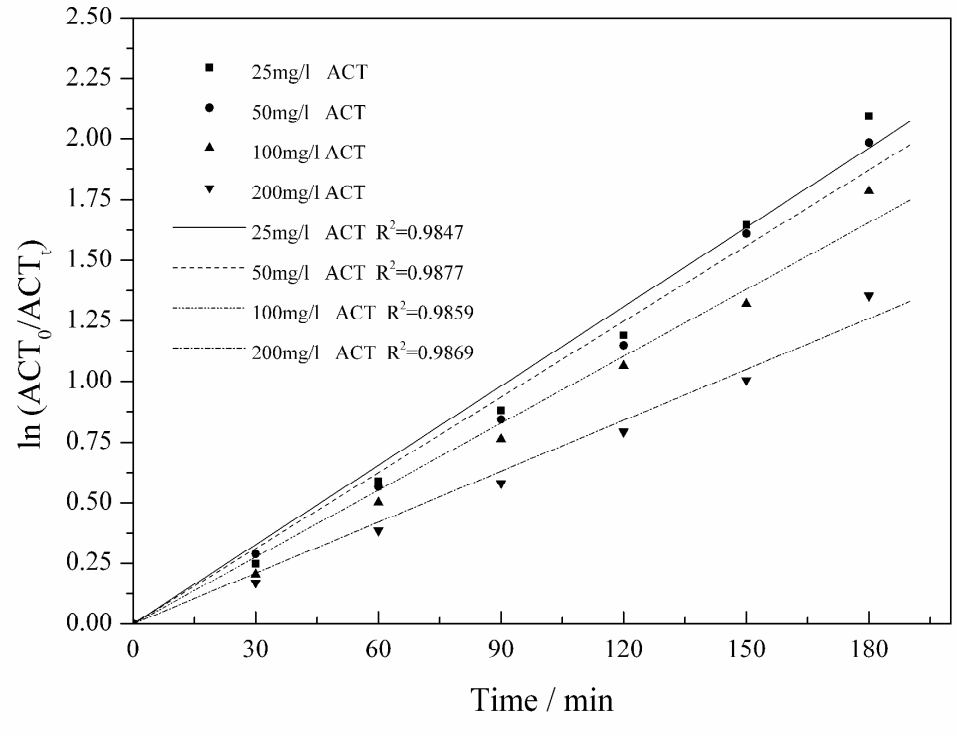

Fig. 8

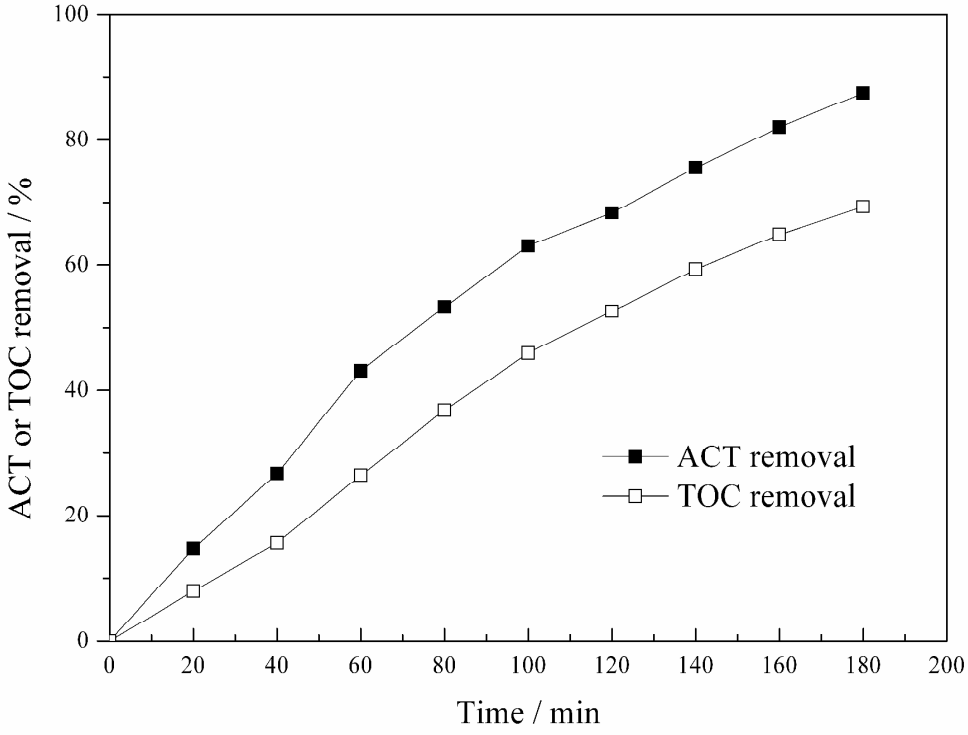

Fig. 9

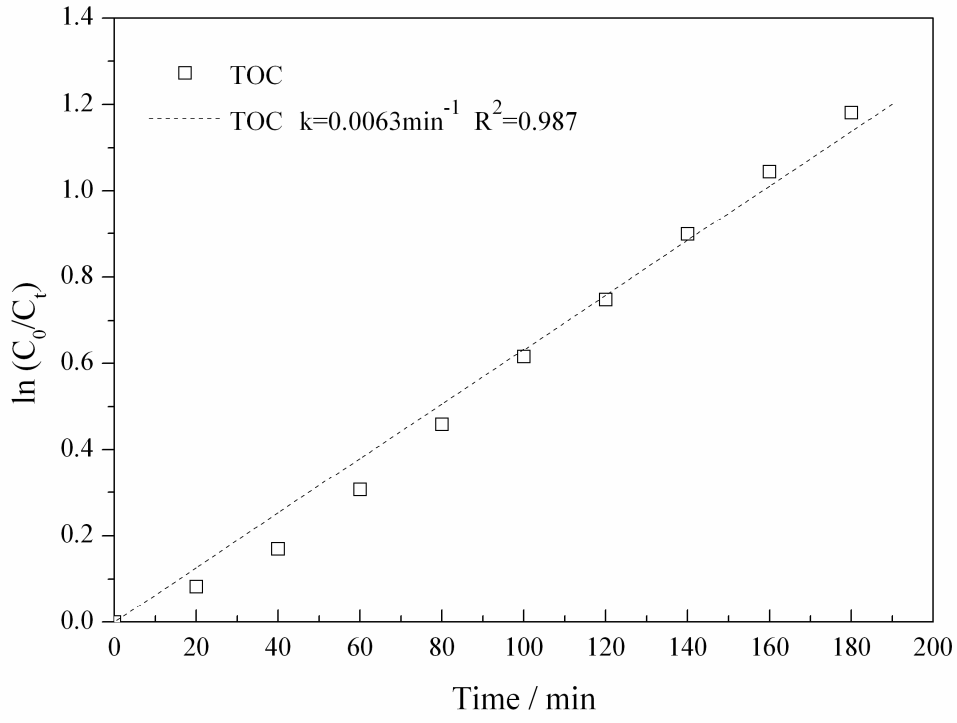

Fig. 10

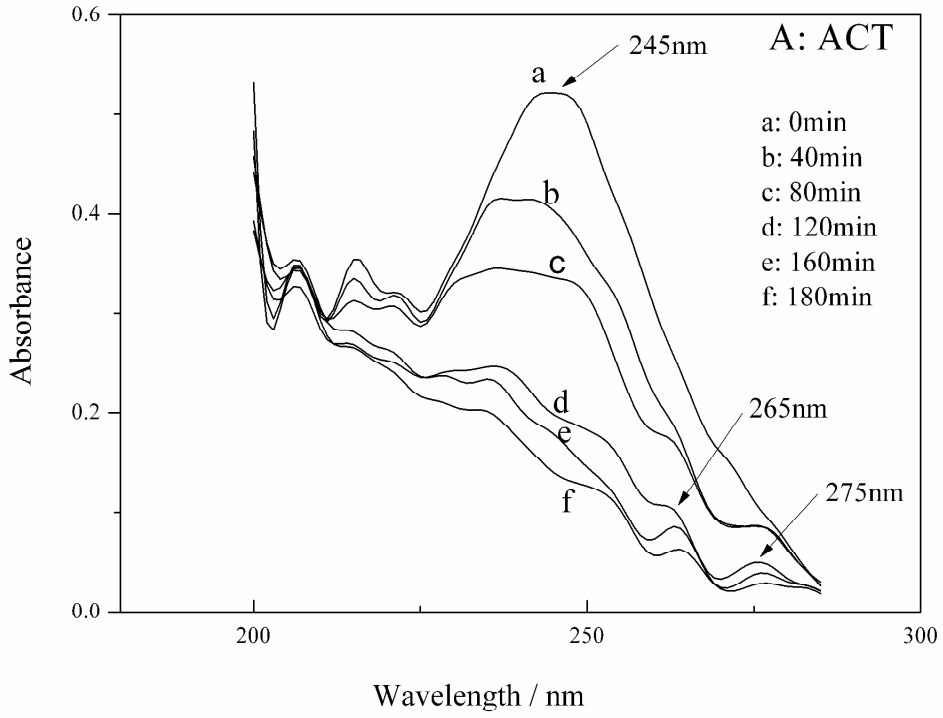

Fig. 11(A)

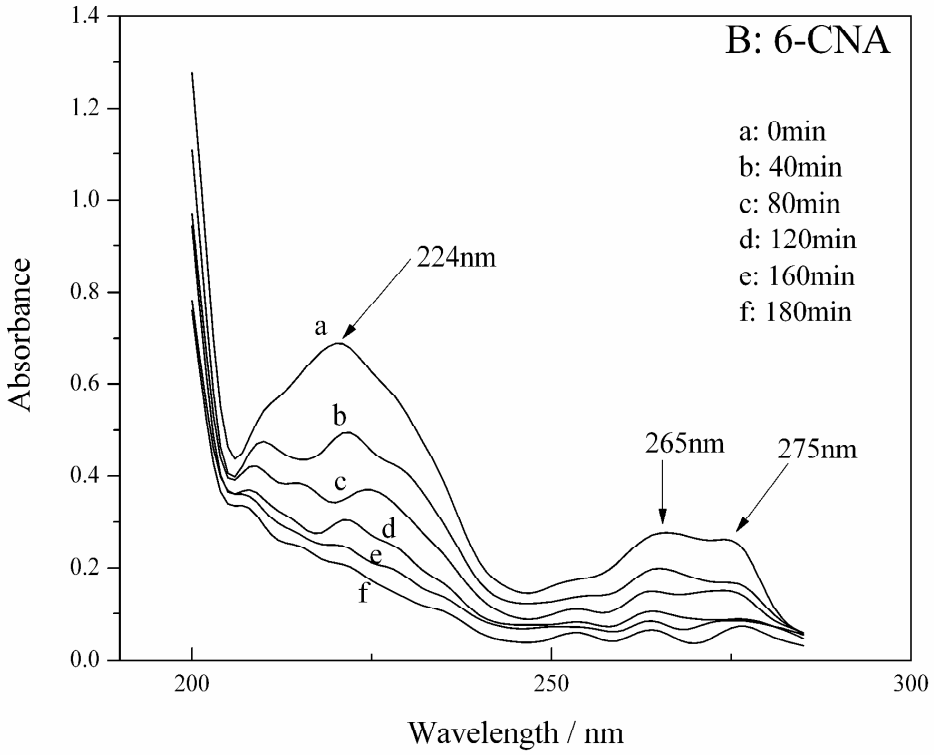

Fig. 11(B)

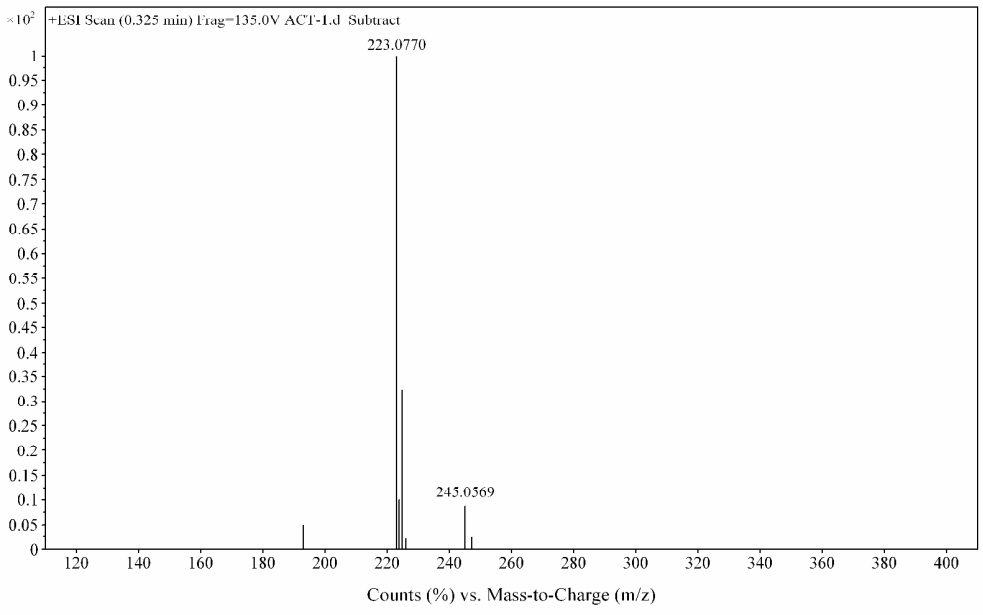

Fig. 12(A)

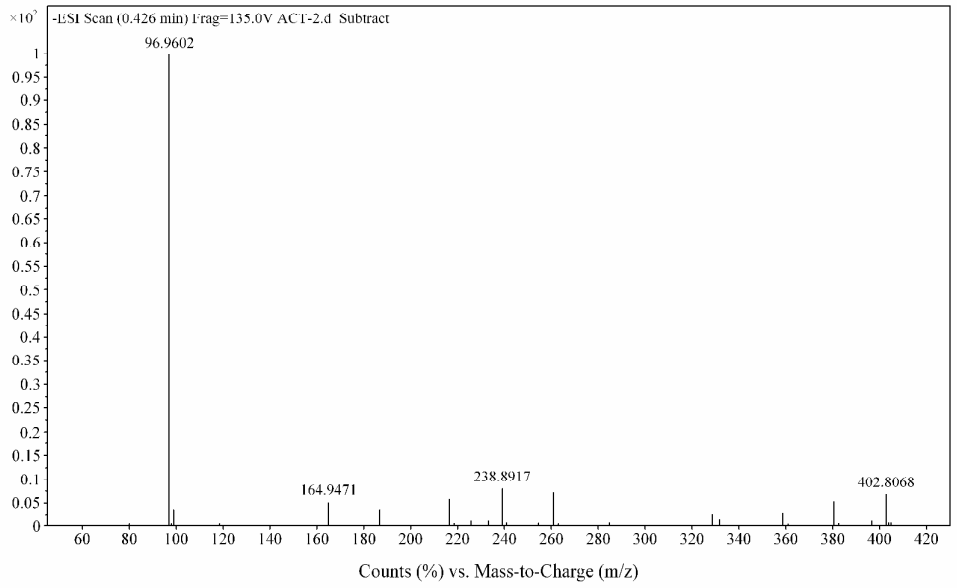

Fig. 12(B)

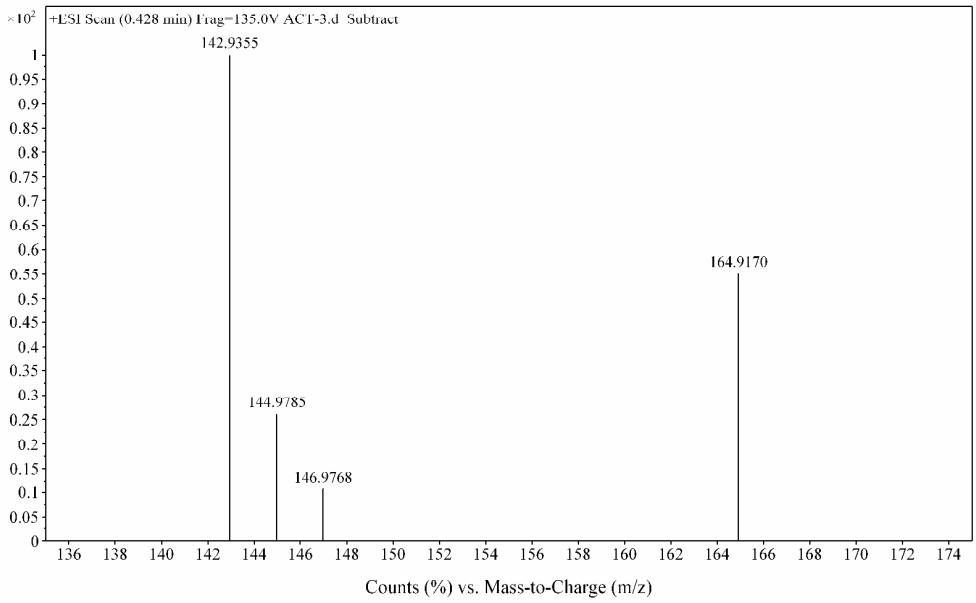

Fig. 12(C)

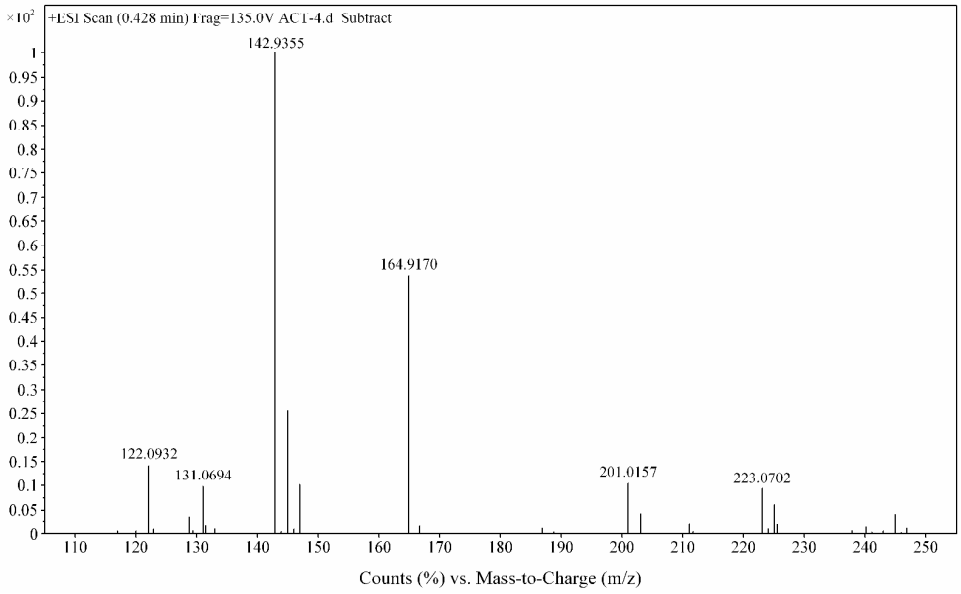

Fig. 12(D)

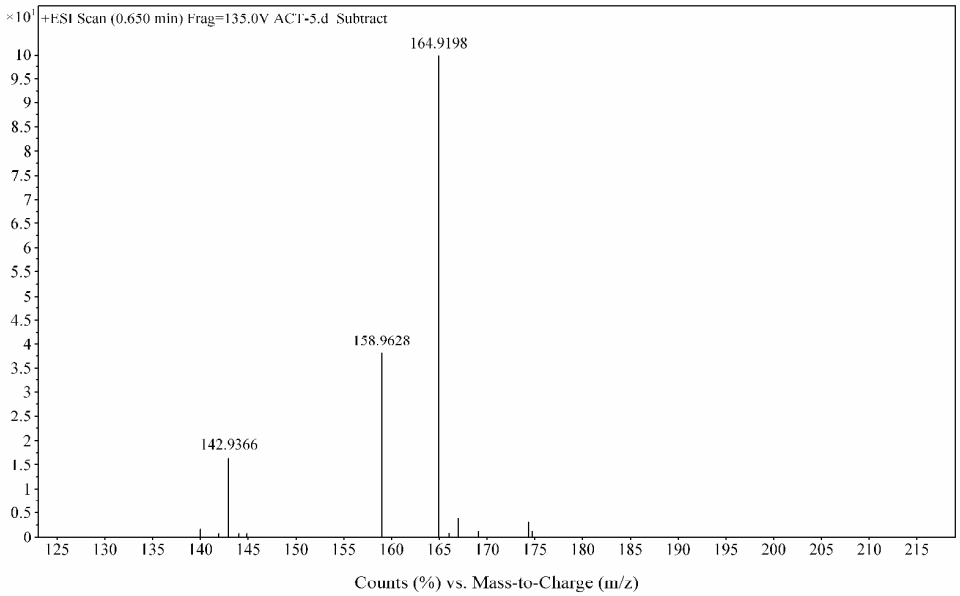

Fig. 12(E)

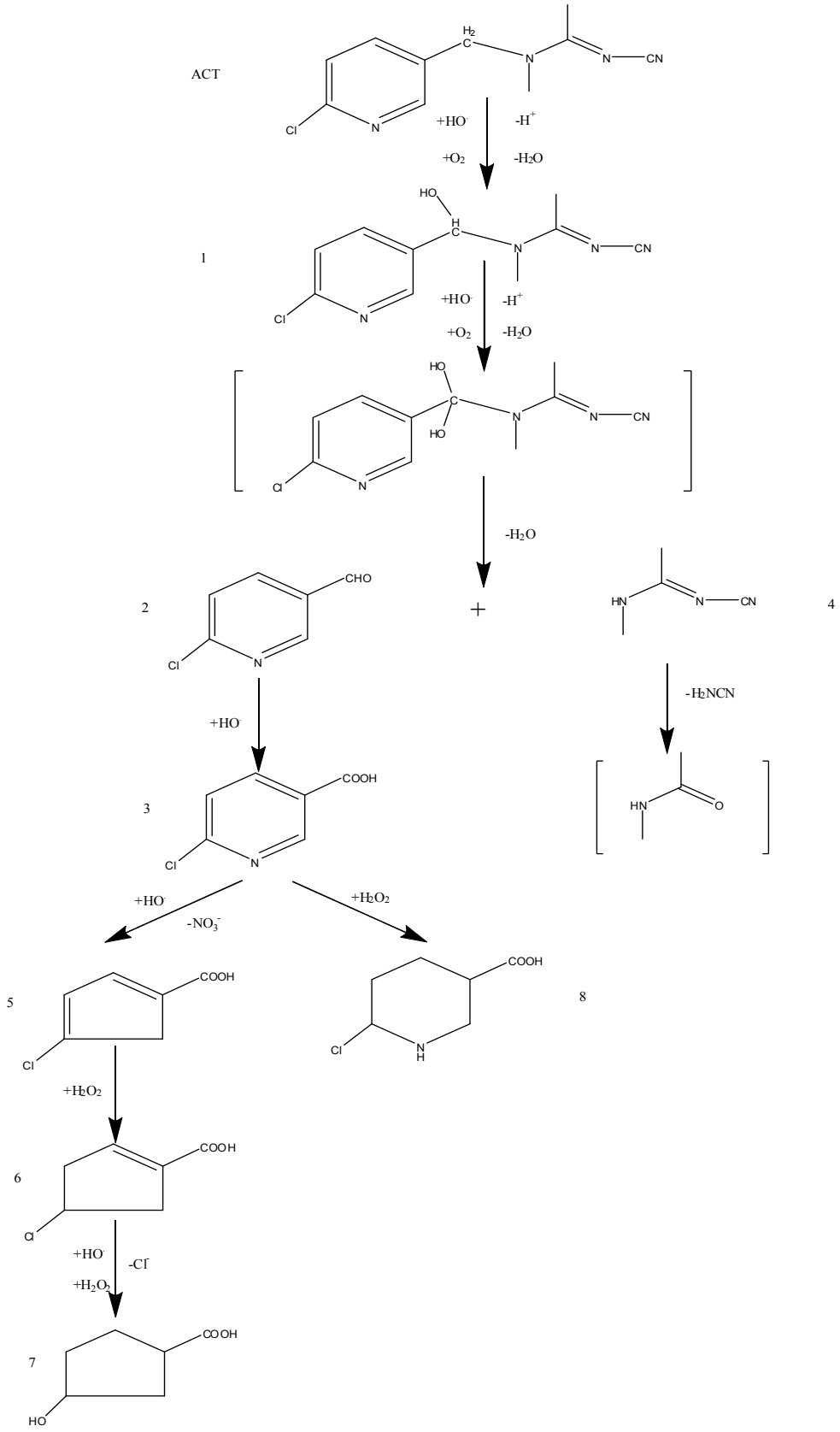

Fig. 13

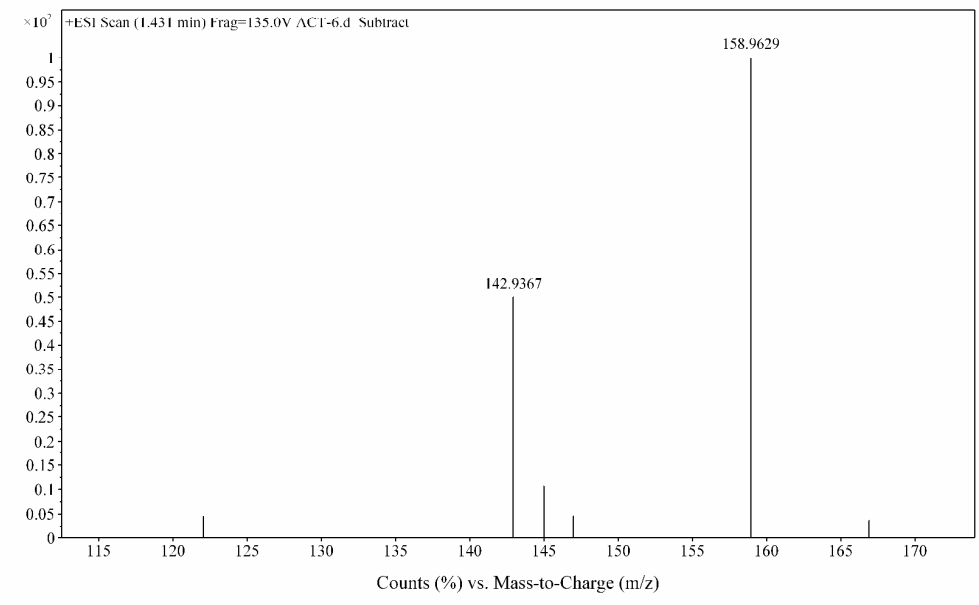

Fig. 14(A)

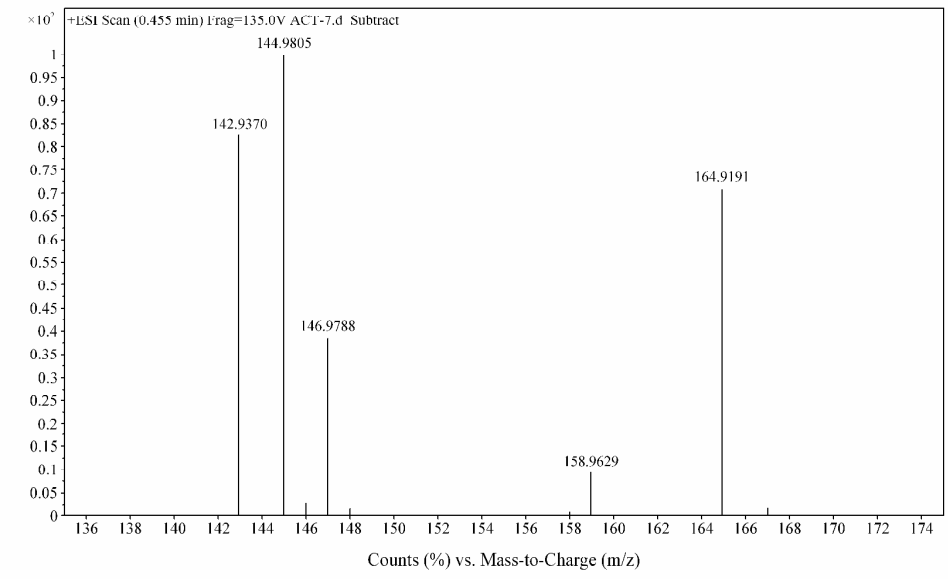

Fig. 14(B)

Table 1

Band gap energies for the Er doped and undoped SnO_2-Sb samples

Samples	Optical absorption threshold λ_g / nm	Band gap E_g / eV
0 mol% Er doped	375	3.31
0.5 mol% Er doped	395	3.14

Table 2

The oxygen evolution reaction kinetic parameters of different electrodes

Electrodes	a / V	b / V
the SnO_2-Sb electrode	1.86019	0.45822
the Er doped SnO_2-Sb electrode	2.15247	0.40721

Table 3

Service life in the accelerated test for different electrodes

Electrodes	Accelerated service life /h	Actual working life / d
Er doped Ti/SnO_2–Sb	18	298
Ti/SnO_2–Sb	8	132

Table 4

The removal amount of ACT and degradation kinetic parameters including $k_{app(ACT)}$ (apparent rate constant), $k_{m(ACT)}$ (mass transport rate) and k_m (apparent mass transfer coefficient) for different initial ACT concentrations

Initial concentration of ACT (mg L^{-1})	25	50	100	200
removal amount (mg L^{-1}) after 180min	21.927	43.134	83.212	148.312
$k_{app(ACT)}$(10^{-4} s^{-1})	1.8167	1.7333	1.5333	1.1667
$k_{m(ACT)}$(10^{-7} $mgm^{-2}s^{-1}$)	0.4646	0.8635	1.4887	2.0185
k_m(10^{-5} ms^{-1})	2.119	2.022	1.789	1.361

Table 5

The source and character of R band, K band and B band

Categories	Origin	Characteristics
R band	Transition from *n* to π^*	Weak absorption, $\lambda_{max} \geqq 270$ nm. If other bands appear, sometimes it shifts to red shift, or be covered with strong absorption band
K band	Especial for conjugated system on transition from π to π^*	Strong absorption, 210 nm $\leqq \lambda_{max} \leqq 270$ nm.
B band	Transition from π to π^* for heterocyclic ring	Moderately strong absorption. The value of B band for pyridine ring is 256 nm.

Table 6

MS data for ACT and several stable degradation intermediate products

Number	Molecular formula	Compounds name	Calculated value of m/z	estimated value of m/z
ACT	$C_{10}H_{11}ClN_4$	(E)-N-((6-chloropyridin-3-yl)methyl)-N'-cyano-N-methylacetimidamide	222.0672	223.0770[M+H]
1	$C_{10}H_{11}ClN_4O$	(E)-N-((6-chloropyridin-3-yl)(hydroxy)methyl)-N'-cyano-N-methylacetimidamide	238.0621	238.8917[M-H]
2	C_6H_4ClNO	6-chloronicotinaldehyde	140.9981	142.9366[M+H]
3	$C_6H_4ClNO_2$	6-chloronicotinic acid	156.9931	158.9628[M+H]
4	$C_4H_7N_3$	(E)-N'-cyano-N-methylacetimidamide	97.0640	96.9602[M-H]
5	$C_6H_5ClO_2$	4-chlorocyclopenta-1,3-dienecarboxylic acid	143.9978	144.9805[M+H]
6	$C_6H_7ClO_2$	4-chlorocyclopent-1-enecarboxylic acid	146.0135	146.9768[M+H]
7	$C_6H_{10}O_3$	3-hydroxycyclopentanecarboxylic acid	130.0630	131.0974[M+H]
8	$C_6H_{10}ClNO_2$	6-chloropiperidine-3-carboxylic acid	163.0400	164.9198[M+H]